INTERNATIONAL JOURNAL FOR NUMERICAL METHODS IN FLUIDS, VOL. 11, 791–809 (1990)

EQUILIBRIUM AND STABILITY OF TOKAMAKS

WOLFGANG KERNER

Max-Planck-Institut für Plasmaphysik, Euratom Association, D-8046 Garching bei München, F.R.G.

SUMMARY

Axisymmetric, ideal MHD configurations with steady flow are computed by the finite-element method. Rectangular elements with four to nine nodes are used. The equilibria are obtained in flux co-ordinates by mesh rearrangement. The properties of the linearized motions around an equilibrium state are studied by a normal-mode analysis. Dissipation is taken into account. Applying the Galerkin method leads to a large-scale complex eigenvalue problem $\mathscr{A}\mathbf{x}=\lambda\mathscr{B}\mathbf{x}$, which is solved by inverse iteration and by the Lanczos algorithm.

1. INTRODUCTION

The objective of controlled thermonuclear fusion research is to derive nuclear energy from the fusion of light nuclei, such as deuterium and tritium, on an economic basis. In order to obtain a sufficient number of fusion processes in a high-temperature laboratory plasma with $T>10$ keV (corresponding to a temperature of 10^8 K), the product of the particle density and the confinement time has to exceed the value given by the Lawson criterion. The concept of magnetic confinement utilizes the fact that the ions gyrate around magnetic field lines, i.e. are tied to the field. Naturally, many instabilities tend to destroy favourable confinement configurations. The tokamak is at present the most advanced reactor concept. The large tokamaks in operation are close to achieving break-even, at which the energy generated equals that necessary to sustain the discharge. In the tokamak device the toroidal current induced in the plasma produces a poloidal magnetic field. Together with the toroidal field, this current yields an equilibrium and also heats the plasma. The principle of the tokamak is shown in Figure 1. The gross macroscopic properties of a laboratory plasma relating to equilibrium, stability and transport are of special interest. Magnetohydrodynamic theory (MHD) is the simplest self-consistent model describing the macroscopic behaviour. This model combines fluid equations with the Maxwell equations. The role of MHD theory is to discover magnetic geometries with favourable equilibrium and stability properties. Neglecting the flow and assuming isotropic pressure yields the well known Grad–Lüst–Schlüter–Shafranov equation for equilibria. Ideal MHD stability of these configurations is considered a necessary condition for successful operation of a tokamak. Dissipative perturbations, especially resistive modes, further reduce the stable region.

Tokamak plasmas exhibit a global time scale, the energy confinement time, of the order of 1 s. In view of the much shorter time scales of instabilities—typical gross ideal MHD instabilities grow in microseconds—the plasma evolves through a sequence of MHD equilibria with good, in the optimum case with complete, stability properties. In the models commonly used, flows are

0271–2091/90/140791–19$09.50 *Received November 1989*

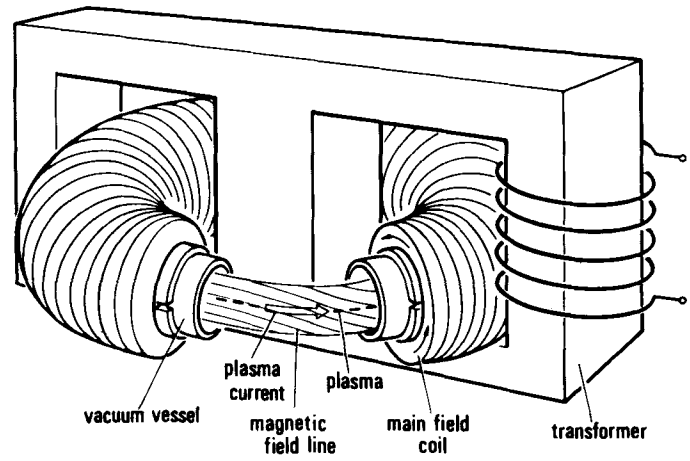

Figure 1. Tokamak schematic. A toroidal current is induced in the plasma, which acts as the second loop of a transformer. This current creates a poloidal magnetic field, which together with the main toroidal field establishes the equilibrium and heats the plasma by ohmic heating

neglected. We have started on an approach for studying equilibria and linear and non-linear evolution of states which takes flows into account.

This paper addresses the numerical solution of tokamak equilibrium and stability. Schemes based on finite elements are especially suited to modelling the geometry in the equilibrium and to yielding high-order resolution in the stability problem. The finite element method is therefore used for the computation of equilibria and for the linear normal-mode analysis. The non-linear simulation is based on finite difference schemes and is not discussed here. The normal-mode analysis is performed in a non-orthogonal flux co-ordinate system and leads to the non-symmetric matrix eigenvalue problem $\mathscr{A}\mathbf{x}=\lambda\mathscr{B}\mathbf{x}$, where the eigenvalue λ is complex. It is emphasized that tokamak equilibria are required to be in flux co-ordinates for stability analysis.

The paper is arranged as follows. Section 2 presents the general MHD model, from which simplified models for equilibrium and stability are derived by making specific assumptions. The numerical solution for tokamak equilibrium and stability is discussed in Section 3. Finally, Section 4 contains the summary and the conclusions.

2. MHD MODEL

The macroscopic plasma behaviour is described by single-fluid theory, where fluid equations are combined with Maxwell's equations. Here the displacement current in Ampère's law is neglected ('pre-Maxwell' equations). The dissipative MHD equations for the density ρ, velocity $\mathbf{u}$, scalar pressure p, temperature T and magnetic field $\mathbf{B}$ in normalized dimensionless form read as follows:

continuity

$$\frac{\partial}{\partial t}\rho+\nabla(\rho\mathbf{u})=0; \tag{1}$$

momentum

$$\rho\left(\frac{\partial}{\partial t}+\mathbf{u}\cdot\nabla\right)\mathbf{u}=-\nabla p+\mathbf{J}\times\mathbf{B}-\nabla\cdot\mathscr{P}+\rho\mathbf{g}; \tag{2}$$

energy

$$\rho\frac{\partial T}{\partial t} = -\rho\mathbf{u}\cdot\nabla T+(\gamma-1)[-p\nabla\cdot\mathbf{u}-\mathscr{P}:\nabla\mathbf{u}+\nabla(\mathscr{K}\cdot\nabla T)]; \tag{3}$$

Maxwell–Ohm

$$\frac{\partial}{\partial t}\mathbf{B}=\nabla\times(\mathbf{u}\times\mathbf{B}-\eta\mathbf{J}); \tag{4}$$

Maxwell

$$\nabla\cdot\mathbf{B}=0, \tag{5}$$

$$\mathbf{J}=\nabla\times\mathbf{B}. \tag{6}$$

The gravitational force $\rho\mathbf{g}$ is important for astrophysical applications, but can be neglected for fusion-relevant laboratory plasmas. The stress tensor $\mathscr{P}$ contains the anisotropic properties of the distribution function. In a strong magnetic field it basically contains parallel and perpendicular pressure components $p_{\|}$ and $p_{\perp}$. In leading order the parallel component of the stress tensor is retained, with only the parallel viscosity coefficient being kept. In the energy equation γ denotes the ratio of the specific heats, which is, as usual, taken equal to 5/3. The dissipative effects are the viscosity μ, the resistivity η and the heat conduction tensor $\mathscr{K}$. The plasma is assumed to be an ideal gas, i.e.

$$p=\rho T. \tag{7}$$

An excellent discussion of MHD theory is given in the books of Bateman[1] and Freidberg.[2]

2.1. Equilibrium

Since both the transport and the resistive time scales are much longer than the ideal Alfven time scale, it is appropriate to model the tokamak equilibrium by ideal MHD.

Let us first recall the case without flow. To compute axisymmetric equilibria, it is convenient to work in cylindrical co-ordinates r, θ, z, with θ being the ignorable co-ordinate. The stationary equations are obtained by setting $\partial/\partial t=0$, and the static equilibrium is given by $\mathbf{u}=0$. Then the equilibrium relation reduces to

$$\nabla p=(\nabla\times\mathbf{B})\times\mathbf{B}, \tag{8a}$$

together with

$$\nabla\cdot\mathbf{B}=0. \tag{8b}$$

The magnetic field is represented as

$$\mathbf{B}=\nabla\theta\times\nabla\psi+F\nabla\theta, \tag{9}$$

where ψ is the poloidal flux and F is the poloidal current profile. Equation (8a) yields that both the pressure and the current profile depend on the flux only, i.e. $p=p(\psi)$ and $F=F(\psi)$. The equilibrium is eventually given by the Grad–Lüst–Schlüter–Shafranov equation for the flux ψ,

$$\nabla\left(\frac{\nabla\psi}{r^2}\right)+\frac{1}{r^2}F\frac{\mathrm{d}F}{\mathrm{d}\psi}+\frac{\mathrm{d}p}{\mathrm{d}\psi}=0, \tag{10}$$

with two arbitrary profiles $p(\psi)$ and $F(\psi)$. Since the plasma boundary is a contour of constant pressure, ψ is constant on the plasma boundary.

We now return to the case with flow. Heating power in the form of neutral beam injection substantially increases the plasma temperature above the level given by the Ohmic heating. Depending on the injection angle, this beam injection generates a flow in both the toroidal and the poloidal directions. The toroidal flow velocities can become quite large, i.e. up to ion sound speed. The magnitude of the poloidal flow is still not accurately determined. Poloidal flow is damped out, thereby increasing transport. This often leads to deterioration of confinement. The stationary equations are again obtained by setting $\partial/\partial t=0$, and the absence of dissipation is expressed by the conservation of the entropy S. The caloric equation of state is

$$p=S\rho^{\gamma} \quad (\gamma=5/3). \tag{11}$$

The continuity equation $\nabla(\rho\mathbf{u})=0$ prompts representation of the velocity as

$$\mathbf{u}=[\Phi(\psi)/\rho]\mathbf{B}+r^2\Omega(\psi)\nabla\theta, \tag{12}$$

where Φ and Ω are flux functions. Note that the radial flow, i.e. diffusion, does not occur in steady-state equilibria. The analysis eventually yields algebraic and differential equations. The solutions for purely toroidal and for general flow are treated separately. Our model treats the temperature as constant along the field lines, i.e. $T=T(\psi)$, in conjunction with purely toroidal flow and as anisotropic when poloidal flow is included. This poloidal flow, although small, is strongly coupled with enhanced radial transport.

For purely toroidal flow the temperature T is a surface quantity, i.e. $T=T(\psi)$, and we obtain, with $\Omega_0=\Omega/\sqrt{T}$,

$$p=p_0(\psi)\exp(r^2\Omega_0^2/2), \tag{13}$$

$$\nabla\left(\frac{\nabla\psi}{r^2}\right)+\frac{1}{r^2}F\frac{\mathrm{d}F}{\mathrm{d}\psi}+\frac{\partial p}{\partial\psi}=0 \tag{14}$$

or

$$\nabla\left(\frac{\nabla\psi}{r^2}\right)+\frac{1}{r^2}F\frac{\mathrm{d}F}{\mathrm{d}\psi}+p\left(r^2\Omega_0\frac{\mathrm{d}\Omega_0}{\mathrm{d}\psi}+\frac{1}{p_0}\frac{\mathrm{d}p_0}{\mathrm{d}\psi}\right)=0. \tag{14b}$$

This equation has the form of the Grad–Lüst–Schlüter–Shafranov equation with arbitrary profiles F, Ω_0, p_0 and T.

The general flow case leads to two algebraic equations

$$F=\frac{I(\psi)+r^2\Phi\Omega}{1-\Phi^2/\rho}, \tag{15}$$

$$H(\psi)=\frac{\Phi^2}{2\rho^2}\mathbf{B}^2-\frac{r^2\Omega^2}{2}+\frac{\gamma}{\gamma-1}S(\psi)\rho^{\gamma-1}, \tag{16}$$

and the differential equation

$$\nabla\left(\frac{(1-\Phi^2/\rho)\nabla\psi}{r^2}\right)+\mathbf{u}\cdot\mathbf{B}\Phi'+\rho\left(r^2\Omega+\frac{F\Phi}{\rho}\right)\Omega'+\frac{1}{r^2}FI'+\rho H'-\frac{1}{\gamma-1}\rho^{\gamma}S'=0, \tag{17}$$

where the prime refers to $\mathrm{d}/\mathrm{d}\psi$. There are now additional functions Φ, I, H and S depending only on ψ. This differential equation is elliptic for

$$0\leqslant\Phi^2/\rho\leqslant\gamma p/(\gamma p+\mathbf{B}^2) \tag{18}$$

and becomes hyperbolic for larger poloidal flow. Since transport estimates imply small poloidal

flow, we shall not be concerned with flows in the hyperbolic domain. There are then no additional difficulties in solving the algebraic equations (15) and (16). It must be ensured, however, that the choice of the free functions does not restrict the solvability, as pointed out in References 3 and 4.

The plasma occupies the domain Γ and is surrounded by vacuum. In order to produce specific plasma boundaries, where the solution satisfies $\psi = \psi_s$ on $\partial\Gamma$, currents in external coils placed in the vacuum region are required. This represents a free surface boundary value problem, where the location and the strength of the individual currents have to be adjusted to produce the desired shape of the plasma cross-section. These techniques are described in Reference 4 and in more detail in Reference 5. Since the vacuum solution B_{vac} and hence ψ_{vac} are not needed for the stability and transport analysis, restriction to the fixed boundary case is possible. The emphasis is then on a high-accuracy solution suitable for the stability analysis. The plasma is thus assumed to be confined within a toroidal, rigid, perfect conductor with the boundary conditions of zero normal components of **u** and **B** at the wall. In the plasma region Γ the differential equation (17) or (14) has to be solved together with the algebraic equations. With the definition

$$k = (1 - \Phi^2/\rho)/r^2 \tag{19}$$

and abbreviation of the other terms by G, $G = G(r, \rho, \psi)$ with $\rho = \rho(r, \psi, |\nabla\psi|)$, we obtain

$$\begin{aligned} \nabla(k\nabla\psi) + G &= 0 \quad \text{in } \Gamma, \\ \psi &= g_1 \quad \text{on } \partial\Gamma_1, \\ \partial\psi/\partial n &= g_2 \quad \text{on } \partial\Gamma_2, \quad \partial\Gamma_1 \cup \partial\Gamma_2 = \partial\Gamma. \end{aligned} \tag{20}$$

The boundary conditions are generalized to Dirichlet and von Neumann conditions.

2.2. Stability

The study of linearized motions has significantly contributed to the understanding of ideal and dissipative MHD plasma phenomena such as stability, wave propagation and heating. The theory of linearized perturbations uses an expansion around a simplified ideal equilibrium with or without flow, as described by equation (20), and linearizes the equations. This is then the place where dissipation is taken into account. The justification for this procedure is given by estimating the time scales of interest. The dissipation introduces finite damping to the motion of ideal MHD. However, the addition of dissipation can produce new instabilities by removing constraints from the ideal model and thereby making states of lower potential energy accessible to the plasma. Owing to the large temperature in a tokamak, the resistivity is quite small. However, the perturbation only needs to break the field in a thin layer within the plasma. If this layer thickness were comparable to the radius of the plasma, the perturbation would only evolve on the diffusion time scale. The perturbation takes into account resistivity in a small layer of width $\delta \propto \eta^{1/3}$ or $\eta^{2/5}$ and connects to the ideal solution further out. The time scales for these instabilities are given by the growth rate $\mathrm{Re}\,\lambda = \lambda_R \propto \eta^{1/3}$ or $\eta^{3/5}$ and are located between the ideal and resistive diffusion time scales. Equally interesting is the question what kind of waves can be sustained in the plasma.

A better understanding is given by estimating the thermal velocity and Alfven velocity for typical parameters ($B \simeq 40$ kG, $T \simeq 2$ keV, $\rho \simeq 10^{14}$ cm^{-3} and $a = 100$ cm):

$$v_{th} \simeq 5 \times 10^7 \text{ cm s}^{-1}, \qquad v_A \simeq 8 \times 10^8 \text{ cm s}^{-1}. \tag{21a}$$

The corresponding time scales are in the microsecond range:

$$\tau_{th} = a/v_{th} \simeq 2 \times 10^{-6} \text{ s} = 2\ \mu\text{s}, \qquad \tau_A = a/v_A \simeq 10^{-7} \text{ s} = 0{\cdot}1\ \mu\text{s}. \tag{21b}$$

The quantities obtained from computations are normalized to the ideal Alfven velocity and ideal Alfven time. The resistive skin time across the plasma radius is

$$\tau_R = a^2/\eta. \tag{22a}$$

The parameter

$$S = \tau_R/\tau_A \tag{22b}$$

is called the magnetic Reynolds number and is of the order of 10^6–10^8 for hot tokamaks. The effect of dissipation on the entire spectrum of normal modes is discussed in detail for two different models, namely the resistive and the non-adiabatic models. The inclusion of resistivity describes perturbations which decouple the plasma from the magnetic field and clearly counteract the concept of magnetic confinement. The non-adiabatic model has zero resistivity but finite heat conductivity and describes, in conjunction with gravity, overstable motion in the convection zone of the Sun. The scheme is easily extended to more general cases such as finite flow in the equilibrium.

All quantities are expanded around the equilibrium in the form

$$f(\mathbf{r}, t) = f_0(\mathbf{r}) + f_1(\mathbf{r}) e^{\lambda t}. \tag{23}$$

The *ansatz* for the temporal dependence in the form of an exponential is suitable for the linearized system where only linear terms in the perturbations are kept. Here λ is the eigenvalue. The imaginary part of λ corresponds to oscillatory behaviour, while a negative real part yields damping and a positive real part an exponentially growing instability.

With resistivity η, gravity $\mathbf{g}$ and thermal conductivity $\mathcal{K}$, the equations for the perturbed quantities ρ, $\mathbf{u}$, T and $\mathbf{b}$ read

$$\lambda\rho = -\nabla\cdot(\rho_0\mathbf{u}), \tag{24a}$$

$$\lambda\rho_0\mathbf{u} = -\nabla(\rho_0 T + T_0\rho) + \rho\mathbf{g} + (\nabla\times\mathbf{B}_0)\times\mathbf{b} + (\nabla\times\mathbf{b})\times\mathbf{B}_0, \tag{24b}$$

$$\lambda\rho_0 T = -\rho_0\mathbf{u}\cdot\nabla T_0 - (\gamma-1)\rho_0 T_0\nabla\cdot\mathbf{u} + (\gamma-1)\nabla(\mathcal{K}_0\cdot\nabla T), \tag{24c}$$

$$\lambda\mathbf{b} = \nabla\times(\mathbf{u}\times\mathbf{B}_0 - \eta_0\nabla\times\mathbf{b}). \tag{24d}$$

The condition $\nabla\cdot\mathbf{b}=0$ is satisfied if $\mathbf{B}_0$ is divergence-free. In one version of our code $\nabla\cdot\mathbf{b}=0$ was used to eliminate b_θ when $\partial_\theta b_\theta \propto m b_\theta \neq 0$, i.e. $m\neq 0$. For the general case a vector potential is introduced by

$$\mathbf{b} = \nabla\times\mathbf{a} \quad \text{and} \quad \mathbf{E} = -\lambda\mathbf{a} - \nabla\Xi. \tag{25}$$

The freedom in the gauge can be used to set the potential Ξ or a specific component of $\mathbf{a}$, e.g. a_r, equal to zero.

Note that no perturbation of the dissipation is taken into account. The system considered is a plasma–vacuum–wall system. To simulate such a system, it is only necessary to give the resistivity in the 'vacuum' a sufficiently large value, and the density, temperature and current small values. The boundary conditions at the wall are

$$\mathbf{n}\cdot\mathbf{u}=0, \qquad \mathbf{n}\cdot\mathbf{b}=0, \qquad \mathbf{n}\times\mathbf{E}=0, \tag{26a}$$

$$\mathbf{n}\cdot\nabla T = 0 \quad \text{if} \quad \kappa_\perp \neq 0. \tag{26b}$$

A state vector $\mathbf{w}$ for the perturbed quantities is introduced:

$$\mathbf{w}^T = (\rho, \mathbf{u}, T, \mathbf{b}).$$

The linear operators in equations (24a–24d) are represented by matrices $\mathscr{R}$ and $\mathscr{S}$, where in $\mathscr{S}$ only the diagonal elements are non-zero and $\mathscr{R}$ contains differential operators and equilibrium quantities. The set of linearized equations then reads

$$\lambda \mathscr{S} \mathbf{w} = \mathscr{R} \mathbf{w}. \tag{27}$$

The ideal MHD spectrum consists of three branches. The spectrum of a typical large-aspect-ratio tokamak case is displayed in Figure 2. The fast magnetoacoustic waves yield a nearly transverse plasma motion, and most of the compression involves the magnetic field and not the plasma. These eigenvalues have an accumulation point at infinity, $\mathrm{Im}\,\lambda \to \infty$, where the radial wave number $k_\perp \propto 1/\Delta r$ becomes large. The second branch is the shear Alfven wave. This wave is also transverse and causes the field line to bend. This mode is incompressible. As is seen from Figure 2, the unstable modes emerge from this branch. The third branch reduces in the small-pressure limit to the sound modes. Note that the Alfven and sound mode branches usually extend to the origin $\lambda = 0$. The ratio of the largest to the smallest eigenvalue thus tends to infinity:

$$\Lambda = \max|\lambda| / \min|\lambda| \to \infty.$$

This indicates that special care is necessary to ensure correct and accurate numerical representation of the entire spectrum. Analytic considerations prompt a special co-ordinate system, so-called 'Hamada' co-ordinates, aligned with magnetic field lines, i.e. in the axisymmetric configurations with magnetic surfaces.

A special system is given by the non-orthogonal co-ordinates ψ, θ, χ with the Jacobian

$$J = \frac{r^2 q(\psi)}{F(\psi)}, \tag{28}$$

where F is defined in equation (9) and $q = q(\psi)$ is the safety factor. Note that in straight cylindrical

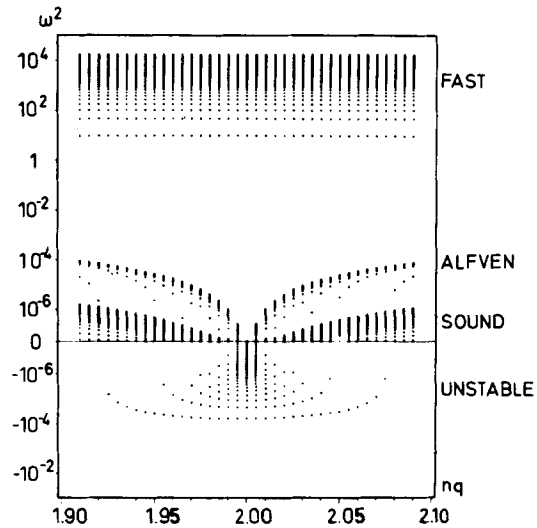

Figure 2. Complete ideal ($\eta \equiv 0$) spectrum of the constant current equilibrium. The square of the eigenvalues ($\lambda = i\omega$) is plotted versus the safety factor with $n = 1$, $m = -2$ and $k = 0{\cdot}1$. Three different branches occur, namely fast magnetoacoustic, Alfven and slow magnetoacoustic waves. Negative values for ω^2 indicate exponentially growing instabilities. The entire spectrum is well resolved and no spurious eigenvalues due to numerical coupling of different branches occur, i.e. no 'pollution'

geometry this system reduces to the usual polar co-ordinates r, θ, z. The ratio of the contravariant components of the magnetic field does not depend on the poloidal angle, i.e. $B^\theta/B^\chi = q(\psi)$. Then the operator $\mathbf{B}\cdot\nabla$ has the form

$$\mathbf{B}\cdot\nabla = B^\theta[\partial_\theta + q(\psi)\partial_\chi].$$

This representation yields considerable simplifications for both analytical and numerical treatment.

3. NUMERICAL SOLUTION

The discussion of the physics showed that two problems have to be solved. First, the equilibrium differential equation for the flux ψ has to be solved and, secondly, a special flux co-ordinate system has to be constructed for every equilibrium. The finite element method is especially well suited to solving both parts because it can be adapted to the special geometry. On the other hand, it allows working in Cartesian co-ordinates, thereby avoiding the singularity at the origin of the inverse equilibrium problem, where r and z are solved as functions of ψ and χ. Consequently, we shall combine the finite element scheme with a mesh refinement procedure, i.e. with an adaptive mesh. According to the discussion of the physical model, two distinct techniques are required for the equilibrium problem and the normal-mode analysis.

3.1. Equilibrium

The differential equation (20) for the magnetic flux is solved by the standard Galerkin procedure. The free functions depending only on ψ can be arbitrarily specified. The Galerkin method uses a linear expansion for ψ, $\psi = \Sigma\,\alpha_i h_i(r, z)$, and solves equation (20) in its weak form. Integration by parts yields the matrix equation for the vector α of expansion coefficients

$$\mathcal{M}\cdot\boldsymbol{\alpha} = \mathbf{b}, \tag{29}$$

where $\mathcal{M}$ denotes the stiffness matrix and $\mathbf{b}$ the force vector:

$$\mathcal{M}_{ij} = \int_\Gamma k\nabla h_i \nabla h_j \,\mathrm{d}\tau, \tag{30}$$

$$b_j = \int_\Gamma G h_j \,\mathrm{d}\tau + \int_{\partial\Gamma_2} k g_2 h_j \,\mathrm{d}\tau + X_j, \tag{31}$$

where X_j expresses the known value of ψ along $\partial\Gamma_1$. The most common two-dimensional finite elements are triangular and rectangular elements. We prefer rectangular elements because they yield more accurate results and are, in addition, better suited to representing the flux contours. Isoparametric mapping provides a one-to-one correspondence between the local (s, t) and the global (r, z) co-ordinates, as is evident from Figure 3. The co-ordinate transformation between the bi-unit square and the curvilinear elements is given by

$$r_m(s, t) = \sum_{i=1}^{9} h_{im}(s, t)\, r_{im}, \qquad z_m(s, t) = \sum_{i=1}^{9} h_{im}(s, t) z_{im}, \tag{32}$$

where (r_{im}, z_{im}) are the global co-ordinates of node i in element m and h_{im} is the interpolation function corresponding to node i of element m. The interpolation functions are defined

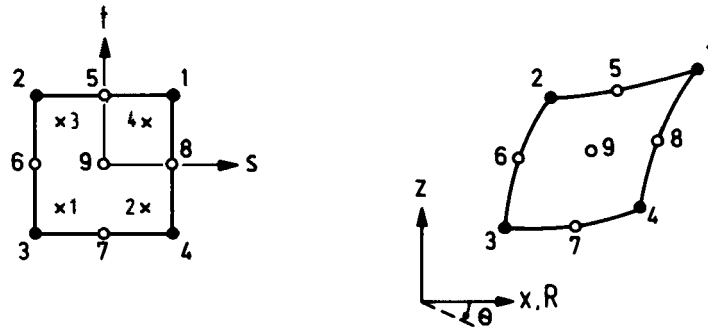

Figure 3. Two-dimensional mapping of four- to nine-node isoparametric element. (a) Bi-unit square in local s–t system. The crosses represent the Gauss point locations for 2×2 integration order. (b) Curvilinear two-dimensional element in global x–y system

as follows:

$$
\begin{aligned}
h_1 &= \tfrac{1}{4}(1+s)(1+t) - \tfrac{1}{2}h_5 - \tfrac{1}{2}h_8 - \tfrac{1}{4}h_9, \\
h_2 &= \tfrac{1}{4}(1-s)(1+t) - \tfrac{1}{2}h_5 - \tfrac{1}{2}h_6 - \tfrac{1}{4}h_9, \\
h_3 &= \tfrac{1}{4}(1-s)(1-t) - \tfrac{1}{2}h_6 - \tfrac{1}{2}h_7 - \tfrac{1}{4}h_9, \\
h_4 &= \tfrac{1}{4}(1+s)(1-t) - \tfrac{1}{2}h_7 - \tfrac{1}{2}h_8 - \tfrac{1}{4}h_9, \\
h_5 &= \tfrac{1}{2}(1-s^2)(1+t) - \tfrac{1}{2}h_9, \\
h_6 &= \tfrac{1}{2}(1-s)(1-t^2) - \tfrac{1}{2}h_9, \\
h_7 &= \tfrac{1}{2}(1-s^2)(1-t) - \tfrac{1}{2}h_9, \\
h_8 &= \tfrac{1}{2}(1+s)(1-t^2) - \tfrac{1}{2}h_9, \\
h_9 &= (1-s^2)(1-t^2),
\end{aligned}
\tag{33}
$$

where the local co-ordinates (s, t) vary in the interval $(-1, 1)$. If the curvilinear element has one or more straight sides, the midside node numbers 5, 6, 7, 8 or 9 corresponding to the straight sides can be omitted by setting the corresponding interpolation functions equal to zero. For details we refer to the book by Bathe.[6]

The same interpolation functions are used to approximate the flux ψ within the element in terms of the value at nodes 1–9:

$$
\psi_m(s, t) = \sum_{i=1}^{9} h_{im}(s, t)\alpha_{im}, \tag{34}
$$

where α_{im} is the value of ψ at the ith nodal point of element m.

The matrix elements $\mathcal{M}_{ij}$, equation (30), and the force vector $\mathbf{b}$, equation (31), are evaluated in 'natural' (s, t) co-ordinates individually for each element. The integration is performed by Gaussian quadratures. We emphasize that the stiffness matrix $\mathcal{M}$ for $\Phi^2/\rho < 1$ is positive definite and of symmetric band form. Efficient solution techniques for the linear system used to solve equation (29) can be applied, these requiring a minimum amount of storage and computing time.[6, 7] On the other hand, a finite difference solution of our problem, equation (20), produces a non-symmetric matrix—a complication additional to the problem of handling the boundary conditions.

The equilibrium equation (20) is highly non-linear and requires iteration for numerical solution. We apply Picard iteration in the form

$$\nabla\{k(\psi^n)\nabla\psi^{n+1}\}+G(\psi^n)=0, \tag{35}$$

where the index n denotes the value of the nth iteration. Note that the relation between ρ and ψ, equation (16), has to be found numerically, i.e. $\rho=\rho(r, \psi^n, |\nabla\psi^n|^2)$. If the flow is purely toroidal, the stiffness matrix is independent of ψ. Thus $\mathcal{M}$ needs to be inverted only once.

The plasma boundary can be arbitrarily specified, e.g. pointwise. From these boundary points and a chosen central point we generate a net of rectangular elements; the innermost ones degenerate into triangles, as shown in Figure 4. As first applications we compute equilibria with up–down symmetry, leading to a Dirichlet condition on the surface and to a von Neumann condition along the $z=0$ plane. The code, of course, is not restricted to such geometries. The plasma behaviour is quite anisotropic with respect to directions along the magnetic field lines and across it. For accurate numerical solution concerning stability and transport it is necessary to use the flux ψ as a variable. Our method shifts the mesh points in the iteration to coincide with surfaces ψ, $\phi=$constant, with ϕ being the poloidal angle of the surface points to the magnetic axis—but it still works in cylindrical co-ordinates. It is easy to transform from the poloidal angle ϕ to the angle χ with straight field lines. It has been pointed out by Grad[8] that the geometry converges faster than the function ψ. In this fashion this scheme is able to provide very accurate equilibrium data in (ψ, θ, χ) co-ordinates efficiently as input for the normal-mode analysis of dissipative MHD.

Results. The first applications of the code serve to test its accuracy. The surface can be specified pointwise or by the analytic representation

$$r=A+\cos(\beta+\delta\sin\beta), \qquad z=K\sin\beta. \tag{36}$$

With up–down symmetry imposed, β varies from zero to $\pi(0\leqslant\beta\leqslant\pi)$. The surface of the case

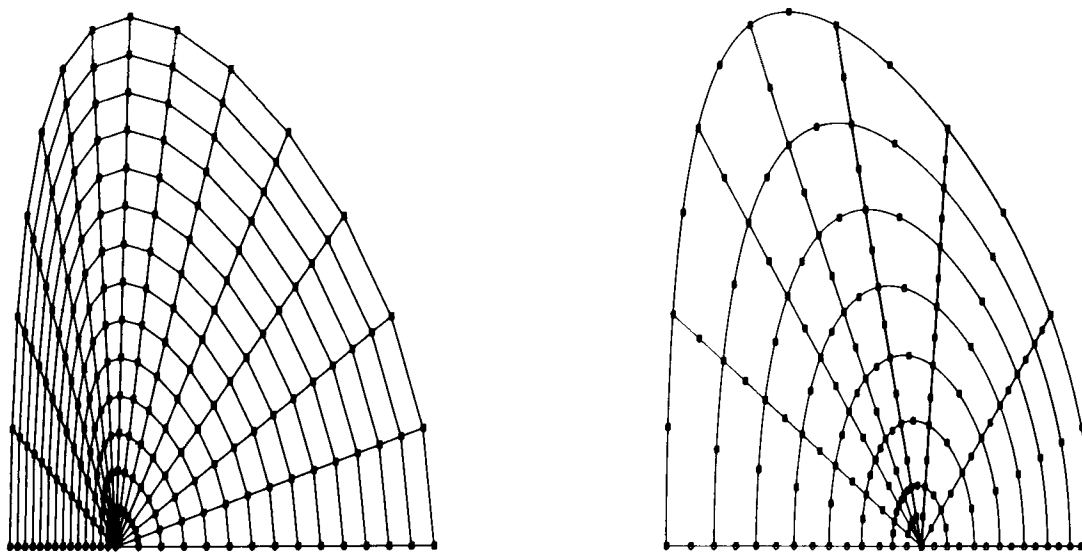

Figure 4. (a) Finite element net ($NR=NP=N=15$) with four-node elements. (b) Finite element net ($NR=NP=N=15$) with eight-node elements coinciding with flux contours

displayed in Figure 4 is defined by $K=2{\cdot}5$, $\delta=0{\cdot}45$ and $A=3{\cdot}0$, which yields an elliptic cross-section with triangularity superimposed. For the four-point elements, shown in Figure 4(a), the mesh is constructed from the surface and an arbitrarily chosen inner point on the z-axis. The eight-node elements in Figure 4(b) coincide with flux contours and display the converged solution.

For constant p' and TT' and zero flow, an exact solution, the Solovev solution (for details see Reference 9), is easily obtained and utilized to test the accuracy of the scheme. The exact solution is normalized such that $\psi(r=0, z=0)=0$ and hence in Figure 5 the error is shown for a varying number of nodal points. For bilinear elements the solution converges as $1/N_t \propto 1/N^2$, where $N_t \approx N^2$ is the total number of grid points, whereas for biquadratic elements the error scales as $1/N_t^2 \approx 1/N^4$. With 41 grid points in both directions the error is then less than 10^{-6}. This accuracy was also confirmed numerically for equilibria with more general non-linear functions $p'(\psi)$ and $TT'(\psi)$. The eight- and nine-node elements yield superior accuracy, since a given surface is better

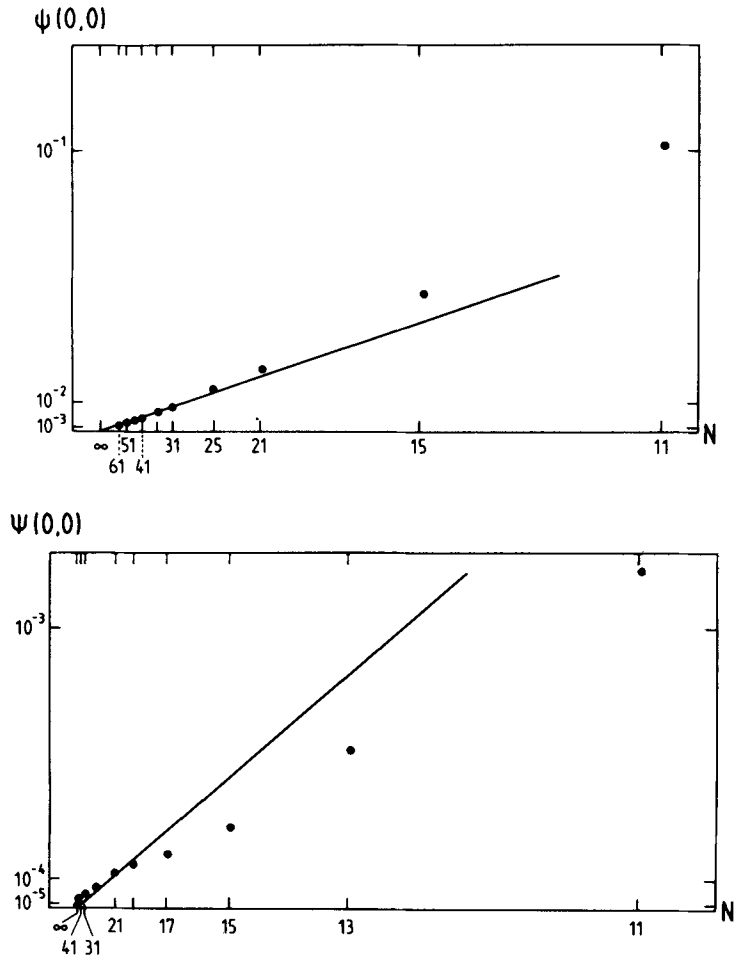

Figure 5. Error of ψ on axis for the constant current case (Solovev equilibrium): (a) for bilinear four-node elements where quadratic convergence in $N(NR=NP=N)$ is obtained; (b) for biquadratic nine-node elements where quadratic convergence in $N(NR=NP=N)$ is obtained

represented. Linear elements underestimate the arc length of a contour, which has to be compensated by a larger number of elements.

Next, the convergence properties in the non-linear equilibrium problem are discussed. Without mesh rearrangement the convergence is fast. After 10 iterations the error—defined as the maximum difference of two subsequent iterations,

$$\varepsilon^n(\psi) = \max |(\psi_{ij}^n - \psi_{ij}^{n-1})/(\psi_a - \psi_s)|, \tag{37}$$

where $\psi_a - \psi_s$ denotes the difference in flux between the axis and the surface—is less than 10^{-5}, as is seen in Figure 6. For this case the surface is specified by the parameters $K = 1{\cdot}5$, $\delta = 0$ and $A = 3{\cdot}0$ in equation (36). The profiles are parabolic ones and are given by

$$p = c_1(\psi - \psi_s)^2 \quad \text{and} \quad F = 1 + d_1(\psi - \psi_s)^2,$$

with $c_1 = 1{\cdot}26 \times 10^{-2}$ and $d_1 = 3{\cdot}92 \times 10^{-2}$.

To represent the equilibrium in flux co-ordinates, the nodal points are rearranged in the iteration to coincide with $\psi = \text{constant}$ contours on rays $\phi = \text{constant}$. A converged result was shown in Figure 4(b). The finite elements are rearranged during the first n_i (in this case $n_i = 3$) iterations and then in steps of n_D (here $n_D = 3$). The iteration is initiated with a constant current. The error of the mesh,

$$\varepsilon^n(\text{mesh}) = \max \{ |r_i^n - r_i^{n-1}|, |z_i^n - z_i^{n-1}| \}/R_a^n, \tag{38}$$

therefore increases in the second iteration but then decreases monotonically to a value below 10^{-4}. The mesh rearrangement introduces an error in ψ, which is seen in the maxima of $\varepsilon(\psi)$ in Figure 6; but in the subsequent iterations the error decreases substantially and is smaller than 10^{-4} at the end of the run. These local maxima in $\varepsilon(\psi)$ are possibly due to the linear interpolation used for convenience in determining the flux contours. The new mesh points are obtained as a superposition of old and new values, e.g.

$$r_i^n = \alpha r_i^n + (1 - \alpha) r_i^{n-1}, \tag{39}$$

to avoid oscillations of the magnetic axis. For the specific case discussed the constant is $\alpha = 0{\cdot}75$. The values of the local maxima and minima of $\varepsilon(\psi)$ occurring in the course of iterations are decreased by a factor of four if the number of mesh points is doubled ($NR = NP = 41$). The local

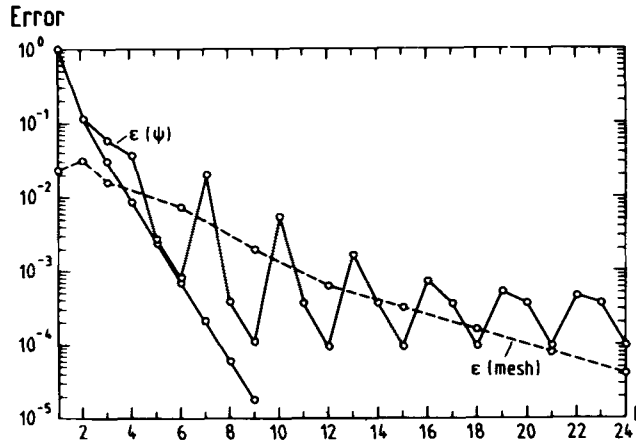

Figure 6. Error of ψ, $\varepsilon(\psi)$, and error of the mesh, ε(mesh), as functions of the number of iterations, n

minima can be made smaller by enlarging the step size for renewing the mesh, e.g. $n_D = 4$. The basic result is that the equilibrium is obtained in flux co-ordinates and is computed with sufficient accuracy. The number of iterations necessary for such an equilibrium is about three times as large as that for a case with fixed mesh.

After convergence the equilibrium is given entirely in flux co-ordinates (ψ, θ, χ) when additional quadratures are performed. The safety factor is evaluated by

$$q(\psi) = \frac{F(\psi)}{2\pi} \oint_{\psi = \text{constant}} \frac{dl}{r|\nabla\psi|}, \tag{40}$$

with $F(\psi)$ introduced in equation (9). The Hamada-like angle χ with corresponding Jacobian $J^{-1} = \nabla\psi \times \nabla\theta \cdot \nabla\chi$, defined in equation (28), is obtained by

$$\chi(r, z) = \frac{F(\psi)}{q(\psi)} \int_0^P \frac{dl}{r|\nabla\psi|}, \tag{41}$$

where the integration is performed on a $\psi = \text{constant}$ contour.

Then at each point (r, z) the values of (ψ, χ) are known and vice versa: $\psi = \psi(r, z)$ and $\chi = \chi(r, z)$. The metric coefficients needed for the normal-mode analysis in the non-orthogonal co-ordinate system (ψ, θ, χ) are $|\nabla\psi|^2$ and $\nabla\psi \cdot \nabla\chi$. Other terms, such as $|\nabla\theta|^2$, are easily evaluated. The remaining coefficient $|\nabla\chi|^2$ is related to $|\nabla\psi|^2$ and $\nabla\psi \cdot \nabla\chi$ through the Jacobian J.

The quantity $|\nabla\psi|$ is required for the quadratures, equations (40) and (41). It is easily evaluated for every element. This immediately presents a problem because ψ is continuous across elements but $|\nabla\psi|$ is not. Additional interpolation is therefore required. It is verified that $|\nabla\psi|$ assumes its minimum error at the Gaussian points indicated in Figure 3. On the basis of these points, $|\nabla\psi|$ is linearly interpolated in r and z across different elements. In this fashion the metric coefficients are evaluated with high accuracy.

A simple multigrid scheme considerably reduces the CPU time. The code is then organized to start with an 11×11 mesh and then to interpolate and to transfer the results for ψ and the flux co-ordinates to a finer grid such as 21×21 or 41×41. Then only a few iterations are required for large systems. It is found that a 21×21 grid is sufficient for most applications and a 41×41 net for the resistive tearing mode stability analysis of the code of Kerner and Tasso.[10] It is estimated that an accurate solution is computed after 30 iterations in about 10–15 s on a CRAY-1S. There is no problem in handling up to 91 radial and poloidal grid points.

3.2. Stability

The numerical procedure for the normal-mode code is described here. The set of linearized MHD equations, equation (24), is solved by the finite element method. In order to reduce the order of derivatives and to obtain the weak form, we take the inner product of the system represented in equation (27) with the weighting function $\mathbf{v}$, which has to be sufficiently regular, and integrate over the plasma volume:

$$\lambda(\mathscr{S}\mathbf{w}, \mathbf{v}) = (\mathscr{R}\mathbf{w}, \mathbf{v}). \tag{42}$$

In the Galerkin method used here the adjoint function satisfies the same boundary conditions as $\mathbf{w}$. A mixed Fourier finite element representation for the state vector is applied in the special co-ordinate system (ψ, θ, χ) adopted to the specific equilibrium considered:

$$\mathbf{w}(\mathbf{r}) = \exp(in\theta) \sum_{m=-\infty}^{m=+\infty} \mathbf{w}_m(\psi) \exp(im\chi). \tag{43}$$

The radial dependence of $\mathbf{w}$ is expressed by a linear combination of local expansion or shape functions. The normal-mode problem exhibits very different spatial and temporal scales, as manifested in the different branches of the spectrum in Figure 2 and in the very localized, almost singular, resistive instabilities. Special care is therefore required in choosing the appropriate numerical approximation for the components of the state vector, $w^j, j=1, 2, \ldots 8$. Optimal numerical approximation of the entire computed spectrum to the true spectrum is obtained if the discretization is chosen to satisfy the following two constraints in every point:

$$\nabla \cdot \mathbf{u} = 0, \tag{44a}$$

$$\nabla \cdot \mathbf{b} = 0. \tag{44b}$$

In ideal MHD the linearized system can be cast as a variational problem for the energy in the Lagrangian displacement ξ, which through $\mathbf{u}=(\partial/\partial t)\xi$ corresponds to the velocity. Uniform convergence of the entire computed spectrum towards the correct spectrum, i.e. good convergence for every eigenvalue, is achieved when the discretization satisfies constraint (44a). Otherwise, pollution is found where a specific eigenvalue converges by increased resolution, but at the same time new incorrect ('polluted') eigenvalues are introduced. It is emphasized that equation (44a) is a constraint for the numerical scheme; the plasma is treated as a compressible medium. Since free functions in the components of $\mathbf{u}$ can be chosen to simplify the divergence, namely to bring it to the form

$$\nabla \cdot \mathbf{u} = (1/J)(\partial u_1/\partial \psi + m u_2 + n u_3),$$

the constraint (44a) implies that the basic functions for u_1, called H, are one order higher in ψ than those of u_2 and u_3, called h:

$$\partial H/\partial \psi = h. \tag{45}$$

This corresponds to a 'staggered' mesh used in finite differences. It is sufficient that $H \in C^0$, i.e. the derivatives need not be continuous.

Dissipative MHD yields a non-variational problem. In order to obtain an equally good numerical approximation, higher-order elements, H, are required for b_ψ. It is found that these functions have to be in C^1, i.e. have to have continuous derivatives. Thus cubic Hermite elements are used for H and quadratic elements for h. No 'spurious' eigenvalues then occur and $\nabla \cdot \mathbf{b}=0$ is satisfied numerically up to machine accuracy. This constraint is now also a physical condition. The spectra computed are again 'pollution-free', as is evident from Figure 2, and high-order convergence, usually better than $1/N_\psi^4$, where N_ψ denotes the number of radial grid points, is achieved. These results are given in Reference 11. This choice for the discretization introduces two orthogonal functions per interval, raising the order of the unknowns in the finite elements to $2N_\psi$ for each component of the state vector $\mathbf{w}$.

The error introduced in the differential equations through the approximation for $\mathbf{w}$ is orthogonal to every expansion function. The Galerkin method eventually leads to the general eigenvalue problem $\mathscr{A}\mathbf{x} = \lambda \mathscr{B}\mathbf{x}$, where the eigenvector contains the coefficients of the expansion functions. The matrix $\mathscr{A}$ is always non-Hermitian—in this formulation even for ideal MHD—and $\mathscr{B}$ is Hermitian and positive definite. The eigenvalue λ and the eigenvector $\mathbf{x}$ of the expansion coefficients, equation (43), are in general complex. The large-scale eigenvalue problem is solved by QR or QZ for all eigenvalues, by the nonsymmetric Lanczos method for a set of eigenvalues[12] and by inverse vector iteration for one eigenvalue at a time.[13] The Fourier finite element expansion leads to a block-tridiagonal structure in the matrices with a block size b,

$$b = 16M, \qquad d = 16MN_\psi, \tag{46}$$

where M is the number of poloidal Fourier harmonics in equation (43), and a total dimension d. For two-dimensional tokamak equilibria, different poloidal Fourier components couple and the dimensions quickly become large, requiring out-of-core storage.[14]

Results. Since the QR and QZ algorithms generate full matrices, only systems up to a dimension $d \approx 1000$ are solved by this method. Even for 1D equilibria with only one Fourier harmonic at a time ($M=1$ in equations (43) and (46)), this is not sufficient for accurate resolution.[11-15] Inverse vector iteration is therefore applied, which preserves the band structure.

Stability with respect to resistive perturbations is discussed in the first application. Here the transition from a purely exponentially growing mode into an exponentially growing and also oscillatory, i.e. overstable, mode is emphasized. The results displayed in Figure 7 are computed by inverse iteration. The parameter α labels the pressure gradient in the equilibrium. For $\alpha > 0{\cdot}868$ two purely exponentially growing modes exist and for $\alpha \to 0{\cdot}868$ these two modes merge to yield a pair of overstable modes for $\alpha < 0{\cdot}868$ with complex conjugate eigenvalues. The matrix dimension for these cases is typically $d=6000$ and the results are numerically converged.

The non-adiabatic model, where the heat conductivity is taken into account in the energy balance, is of relevance for astrophysical studies relating to solar and stellar plasmas. The combined action of gravity and heat conductivity yields overstable modes. A typical result is shown in Figure 8. Again, pairs of purely exponentially growing modes merge and form pairs of overstable modes with complex conjugate eigenvalues. The oscillatory frequency of the modes approaches the isothermal frequency, i.e. $\lambda = i\omega_I$, where

$$\omega_I^2 = \frac{p}{p+\mathbf{B}^2}\omega_A^2 \quad \text{with} \quad \omega_A^2 = (\mathbf{k}\cdot\mathbf{B})^2/\rho, \tag{47}$$

with the wave vector $\mathbf{k}$, and not the Alfven frequency $\lambda = i\omega_A$ as was previously assumed. In this example the instabilities form a curve in the complex λ-plane extending from the real λ-axis to the imaginary axis. These eigenvalues were computed successively by inverse iteration. For details we refer to Reference 16.

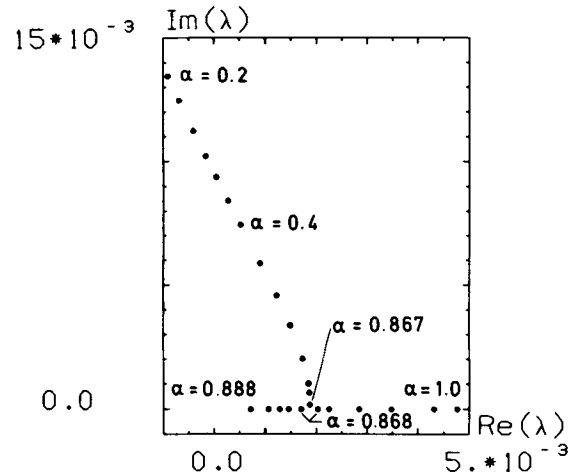

Figure 7. Overstable modes for a tokamak-like equilibrium with varying pressure gradient. The values of α, which governs dp/dr, are given. The parameters are $\eta = 2 \times 10^{-5}$, $n=1$, $m=-2$ and $k=0{\cdot}2$. Re λ denotes the growth rate and Im λ the oscillation frequency. For decreasing values of α, two unstable, purely exponentially growing modes merge to yield complex eigenvalues for $\alpha < 0{\cdot}868$

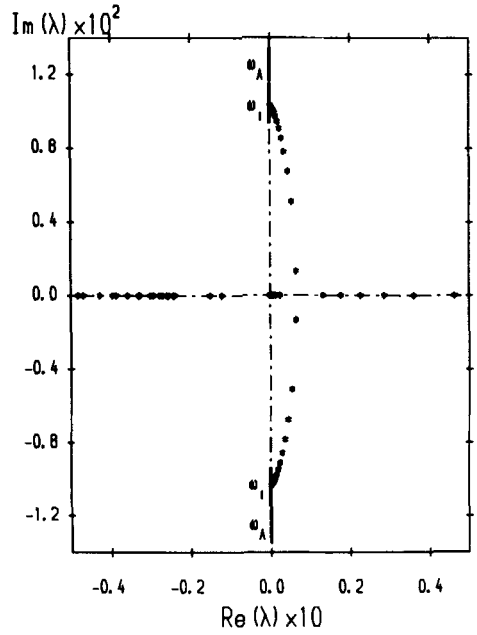

Figure 8. Overstable modes in the convection zone of stars in the presence of a magnetic field, where heat conduction and gravity is taken into account

The normal-mode analysis for 2D equilibria results in large matrix dimensions $d > 10^4$. There is then a great need for a solver which preserves the sparseness—at least the band width—and which produces a subset of the spectrum. We propose the Lanczos algorithm for this purpose. A specific non-symmetric Lanczos scheme with no reorthogonalization was implemented.[12] When it was applied to resistive MHD, we were able to compute entire branches in one computer run. The resistive Alfven spectrum is presented in Figure 9 and the resistive Alfven sound spectrum in Figure 10, as computed simultaneously by means of the Lanczos scheme. These results compare extremely well with those computed successively by inverse iteration. With respect to storage requirements, the Lanczos scheme utilizes the same matrices in band matrix storage mode as does the inverse vector iteration.

These results demonstrate that the normal-mode analysis arising from quite different dissipative MHD models is solved with great accuracy.

The normal-mode code for general two-dimensional axisymmetric equilibria has been completed. This includes computation of equilibria together with evaluation of the metric quantities in the adapted flux co-ordinate system, as described above. The program has been successfully tested for ideal MHD in the case of the Solovev equilibrium. Dissipative spectra have also been correctly evaluated. These results involving convergence studies with respect to the number of poloidal Fourier harmonics and with respect to the number of radial finite elements will be given elsewhere.

4. DISCUSSION

An approach for analysing equilibrium, stability and transport of macroscopic tokamak plasmas where flows and dissipation are taken into account has been presented. The plasma behaviour is

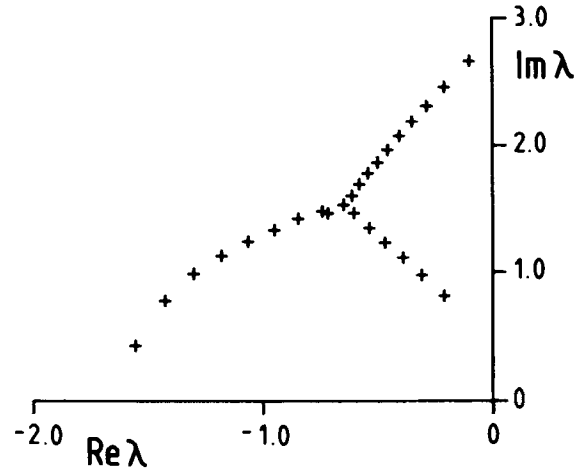

Figure 9. The resistive Alfven spectrum for an equilibrium with linear profiles and pressure set to zero. The solid bar on the imaginary axis denotes the ideal Alfven continuum ($0{\cdot}40 \leqslant \mathrm{Im}\,\lambda_{id} \leqslant 2{\cdot}80$). For $\eta = 5 \times 10^{-5}$ and $N = 375$ intervals ($d = 4498$), simultaneously evaluated by the Lanczos scheme with no orthogonalization. All eigenvalues are converged and agree very well with those successively computed by inverse vector iteration

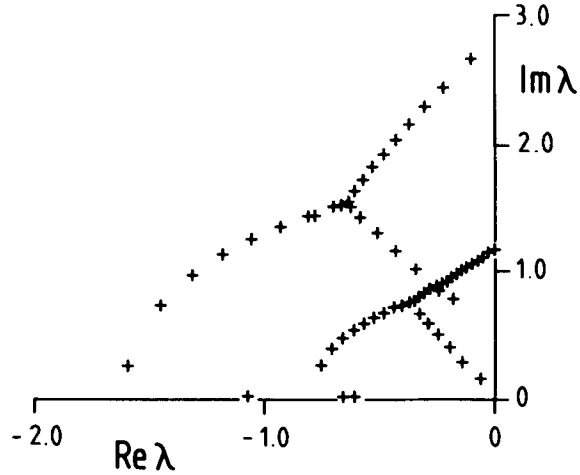

Figure 10. The resistive Alfven and cusp spectrum for an equilibrium with linear profiles and finite pressure. The ideal Alfven and slow mode continua overlap. The solid bar on the imaginary axis denotes the ideal Alfven continuum ($0{\cdot}40 \leqslant \mathrm{Im}\,\lambda_{id} \leqslant 2{\cdot}80$). For $\eta = 6 \times 10^{-5}$ and $N = 375$ intervals ($d = 4498$), simultaneously evaluated by the Lanczos scheme with no orthogonalization. All eigenvalues are converged and agree very well with those successively computed by inverse vector iteration

quite anisotropic with respect to directions along the magnetic field line and across it. Any numerical scheme has to be tailored accordingly. A good description is achieved by utilizing special non-orthogonal flux co-ordinates (ψ, θ, χ). Consequently, the geometry of these flux contours as well as specifically prescribed boundaries have to be well resolved. Finite elements are especially well suited to solving such problems accurately.

The non-linear equilibrium equation is solved by applying two-dimensional rectangular finite elements with up to nine nodes per element. These nodal points are arranged to coincide with the

flux contours. Superior resolution is obtained by biquadratic elements with eight or nine nodal points, as compared with bilinear four-point elements. These high-order elements yield quartic convergence with respect to the number of radial and poloid grid points $NR = NP = N$. The mapping into the flux co-ordinate system is completed by performing quadratures along ψ = constant contours for evaluation of the required metric tensor elements. Here the derivatives of ψ have to be interpolated across different elements in order to make $|\nabla\psi|$ continuous everywhere. It is concluded that two-dimensional cubic Hermite elements with continuous derivatives across different elements should yield better representation together with higher accuracy. The difficulty of performing the isoparametric mapping for such elements is well known and has to be appropriately taken into account.

In the next step the equations are linearized around an equilibrium state. Here dissipation is usually taken into account. The normal-mode analysis is based on a Fourier expansion in the poloidal angle and a finite element expansion in the radial direction. This allows good resolution of small layers with steep gradients across specific radial flux contours, so-called resonant surfaces. A proper numerical approximation of the entire spectrum is aimed at, i.e. homogeneous convergence of the entire numerically computed spectrum to the true spectrum when the resolution is increased. It is established that very good numerical accuracy is achieved when a mixture of cubic Hermite and quadratic finite elements is applied. The components of the state vector are expanded into these two different sets of expansion functions in such a way that specific numerical constraints can be satisfied. This allows correct representation of the relevent operators $\nabla \cdot \mathbf{u}$ and $\nabla \cdot \mathbf{b}$.

The normal-mode analysis leads to a large-scale complex eigenvalue problem. Only for small systems with dimensions of up to $d \approx 1000$ are the corresponding matrices diagonalized by the QR or QZ algorithm. For larger systems the eigenvalues are computed by inverse vector iteration and by the Lanczos algorithm, where the band structure of the matrices is preserved. In conjunction with out-of-core storage, large systems with dimensions of up to $d \approx 100\,000$ can be solved for. Extremely interesting eigenvalue patterns have been derived. The spectrum of resistive Alfven modes of a static cylindrical plasma equilibrium has been analysed in detail. At present this code is being applied to fully 2D equilibria without flow. More details are given in References 11–15.

We may wish to design a general scheme for the equilibrium problem and the normal-mode analysis. In both cases cubic Hermite expansion functions would be preferred. Thus we propose using two-dimensional elements with cubic Hermite expansion functions in conjunction with an adaptive mesh. Such a scheme may also be applied to the corresponding non-linear MHD simulation, which has so far been done basically by finite difference discretization.

The Hermitian eigenvalue problem has all the good properties to ensure successful numerical evaluation, since a Hermitian matrix cannot be defective and since a small perturbation in the matrices causes only a small perturbation in the eigenvalues. On the other hand, the non-symmetric eigenproblem yields intrinsic obstacles. Not every general matrix can be diagonalized, but even for non-defective matrices the error propagation can cause severe numerical problems. Therefore the solution for the eigenvalues of a general non-variational problem is a major achievement! As a test case we solved the ideal MHD spectrum shown in Figure 2 by a non-variational formulation involving non-symmetric matrices and obtained excellent agreement with the results obtained from a variational formulation with symmetric matrices. Inverse iteration performs quite similarly for symmetric and non-symmetric problems.

In the case where appropriate discretization is achieved, high accuracy is found for the solution of the general system. Accurate resolution of instabilities with very small growth rates, such as $\mathrm{Re}\,\lambda \approx 10^{-6}$, is found, whereas for the Hermitian case $-\omega^2 \approx 10^{-6}$ corresponding to $\mathrm{Re}\,\lambda \approx 10^{-3}$ is close to the limit. Hence enlarging the system from three to six (actually to eight) unknowns in the

state vector but keeping only first derivatibes with respect to time seems to improve the accuracy considerably.

A final question may be: how accurately are the stability limits of general two-dimensional configurations determined? The point $\lambda \equiv 0$ or $\mathrm{Re}\,\lambda = 0$ is, of course, influenced by all kinds of errors, especially by errors in the equilibrium and in the mapping. A consistent formulation for equilibrium and stability, such as discussed above, keeps these errors small. Since derivatives of the metric tensor elements of the non-orthogonal co-ordinate system are involved, the second derivatives of ψ are involved and, consequently, the difference between the left-hand and right-hand sides of the discretized equilibrium relation (20). This error can be made small by employing sufficiently many grid points or by utilizing higher-order finite elements. The importance of the accuracy in the second derivative in the solution ψ gives another argument in favour of proposing bicubic elements in the future.

The stability analysis is usually done by applying a continuation procedure using a relevant physical quantity, such as the ratio of the total plasma pressure to the magnetic pressure, the plasma beta. Then an eigenvalue is traced from the unstable region to the stable region. The transition point $\lambda \equiv 0$ is thus better determined. The experience from the ideal MHD stability calculations is that the points of marginal stability, the 'beta limit', can be determined within a margin of 10%. With increased resolution this tolerance can be made even smaller, namely to about 5%. Then a given beta limit of $\beta = 5\%$ has to be read as $\beta = (5 \pm 0.5)\%$ or $(5 \pm 0.2)\%$.[17] This is fully sufficient for interpreting the present results and for designing new devices.

REFERENCES

1. G. Bateman, *MHD Instabilities*, MIT Press, Cambridge, MA, 1978.
2. J. P. Friedberg, *Ideal Magnetohydrodynamics*, Plenum, New York, 1987.
3. S. Semenzato, R. Gruber and H. P. Zehrfeld, *Comput. Phys. Rep.*, **1**, 389 (1984).
4. W. Kerner and S. Tokuda, *Z. Naturforsch.*, **42a**, 1154 (1987).
5. K. Lackner, *Comput. Phys. Commun.*, **12**, 33 (1976).
6. K. Bathe, *Finite Element Procedures in Engineering Analysis*, Prentice-Hall, Englewoods Cliffs, NJ, 1982.
7. W. Kerner and O. Jandl, *Comput. Phys. Commun.*, **31**, 269 (1984).
8. H. Grad, *Courant Institute Report MF-93 (COO-3077-154)*, October 1978.
9. W. Kerner, *Nucl. Fusion*, **16**, 643 (1976).
10. W. Kerner and H. Tasso, *Phys. Rev. Lett.*, **49**, 654 (1982).
11. W. Kerner, K. Lerbinger, R. Gruber and T. Tsunematsu, *Comput. Phys. Commun.*, **36**, 225 (1985).
12. J. Cullum, W. Kerner and R. A. Willoughby, *Comput. Phys. Commun.*, **53**, 19 (1989).
13. W. Kerner, K. Lerbinger and J. Steuerwald, *Comput. Phys. Commun.*, **38**, 27 (1985).
14. W. Kerner, E. Schwarz and J. Steuerwald, in J. Nührenberg (ed.), *Proc. 8th Europhysics Conf. on Computational Physics*, Eibsee, 1986, 10D, pp. 83–85.
15. W. Kerner, in J. Cullum and R. A. Willoughby (eds), *Large Scale Eigenvalue Problems*, Elsevier/North-Holland, Amsterdam, 1986, p. 241.
16. D. Hermans, M. Goossens and W. Kerner to be published.
17. A. D. Turnbull and F. Troyon, *Comput. Phys. Commun.*, **52**, 303 (1989).